Energy production and self-sustained turbulence at the Kolmogorov scale in Couette flow

Qiang Yang[1,3], Ashley P. Willis[2], Yongyun Hwang[1],†

[1]Department of Aeronautics, Imperial College London, South Kensington, London SW7 2AZ, UK

[2]School of Mathematics and Statistics, University of Sheffield, S3 7RH, UK

[3]School of Engineering and Centre for Scientific Computing, University of Warwick, Coventry CV4 7AL, UK

(Received xx; revised xx; accepted xx)

Several recent studies have reported that there exists a self-similar form of invariant solutions down to the Kolmogorov microscale in the bulk region of turbulent Couette flow. While their role in a fully-developed turbulent flow is yet to be identified, here we report that there exists a related mechanism of turbulence production at the Kolmogorov microscale in the bulk region of turbulent Couette flow by performing a set of minimal-span direct numerical simulations up to friction Reynolds number $Re_\tau \simeq 800$. This mechanism is found to essentially originate from the non-zero mean shear in the bulk region of the Couette flow, and involves the eddy turn-over dynamics remarkably similar to the so-called self-sustaining process (SSP) and/or vortex-wave interaction (VWI). A numerical experiment that removes all the other motions except in the core region is also performed, which demonstrates that the eddies at a given wall-normal location in the bulk region are sustained in the absence of other motions at different wall-normal locations. It is proposed that the self-sustaining eddies at the Kolmogorov microscale correspond to those in uniform shear turbulence at transitional Reynolds numbers, and a quantitative comparison between the eddies in uniform shear and near-wall turbulence is subsequently made. Finally, it is shown that the turbulence production by the self-sustaining eddies at the Kolmogorov microscale is much smaller than that of full-scale simulations, and that the difference between the two increases with Reynolds number.

1. Introduction

The discovery of unstable invariant solutions of the Navier–Stokes equations, such as stationary/traveling waves and periodic orbits, has led to significant advancement in the understanding of transition and turbulence at low Reynolds numbers. Many of these solutions have been found in wall-bounded shear flows, such as plane Couette, pressure-driven channel and pipe flows, and boundary layer (e.g. Nagata 1990; Waleffe 2001; Kawahara & Kida 2001; Faisst & Eckhardt 2003; Wedin & Kerswell 2004; Hall & Sherwin 2010; Park & Graham 2016, and many others). These invariant solutions form a state-space skeleton (Gibson *et al.* 2008; Willis *et al.* 2013, 2016), and their understanding from a dynamical systems viewpoint has played the key role in illuminating the nature of bypass transition and low-Reynolds-number turbulence. It has also recently been shown that computation of these invariant solutions with a suitable modelling of surrounding small-scale turbulence may also be relevant to the description of large-scale coherent

† Email address for correspondence: y.hwang@imperial.ac.uk

structures emerging at much higher Reynolds number (Rawat, Cossu, Hwang & Rincon 2015; Hwang, Willis & Cossu 2016).

Recently, several researchers have discovered a self-similar form of some invariant solutions in the core region of plane Couette flow with respect to the given spanwise length scale (Blackburn, Hall & Sherwin 2013; Deguchi 2015; Eckhardt & Zammert 2016). In particular, Deguchi (2015) showed that the smallest possible invariant solutions emerge at Kolmogorov microscale using an asymptotic theory. These findings are very intriguing, as the self-similar nature of the invariant solutions down to Kolmogorov scale is seemingly reminiscent of the eddy structures expected in the Richardson-Kolmogorov energy cascade (Kolmogorov 1941, 1991). However, it should be pointed out that the energy cascade is also a well-established concept in turbulent flows even without any mean shear (isotropic turbulence) (see e.g. Vassilicos 2015), whereas the invariant solutions, at least of the type mentioned here, would not exist in the absence of mean shear.

Indeed, the question of whether or not there exists a link between the self-similar invariant solutions and the eddies in the energy cascade is very puzzling. On the one hand, the invariant solutions have often been understood to underpin a sustaining mechanism of energy-carrying eddies (i.e. coherent structures) via the so-called self-sustaining process (SSP) (Hamilton *et al.* 1995; Waleffe 1997) and/or vortex-wave interaction (VWI) (Hall & Smith 1991; Hall & Sherwin 2010). This process is essentially a two-way interaction between wavy streaks and streamwise vortices, and, in particular, the amplification process of streaks by streamwise vortices (i.e. 'lift-up' effect) involves production of turbulent kinetic energy – the production term in the standard turbulence budget equation has the same mathematical origin with the off-diagonal term in the Orr-Sommerfeld and Squire equations that represents the lift-up effect (Hwang 2016). On the other hand, when considering the cascade, the Kolmogorov microscale is essentially derived by considering the scale, at which the rate of 'energy transfer' from large scale (equivalent to the rate of turbulence dissipation) is expected to be balanced with viscous dissipation (Kolmogorov 1941, 1991). Therefore, the eddies at Kolmogorov scale in the energy cascade should be mainly driven by the energy transferred from large scales. However, for invariant solutions the energy production and dissipation are in perfect balance on the scale of the structure. Also, in general, not all eddies at Kolmogorov microscale are the outcome of the energy cascade in a high-Reynolds-number turbulent flow. An important example of this is the near-wall turbulence in and below the buffer layer. The integral length scale in this region is the viscous inner length scale $\delta_\nu = \nu/u_\tau$ (ν is the kinematic viscosity and u_τ is the friction velocity), and this is identical to the corresponding Kolmogorov length scale.

Motivated by this puzzling issue, the goal of the present study is to report our observation that there exists a turbulence production mechanism at the Kolmogorov microscale in the bulk region of turbulent Couette flow, where the invariant solutions at Kolmogrov microscale have been found (e.g. Deguchi 2015). This mechanism is found to essentially originate from the uniform local mean shear in the flow, and, interestingly, we shall see that the related eddy turn-over dynamics is remarkably similar to the SSP/VWI. A numerical experiment, that removes all the structures except those in the core of the channel, is also performed, and we demonstrate that the energy-producing structures in the bulk region sustain themselves, suggesting that the invariant solutions at the Kolmogorov microscale are likely to underpin the dynamics of these structures. Finally, it should be mentioned that, given the definition of the Kolmogorov microscale, dissipation of the energy produced by these self-sustaining structures must take place at the same scale, thereby consistent with the nature of the invariant solutions that exhibits perfect balance between production and dissipation on the scale of structure.

2. Background

2.1. *Mean-momentum balance*

We consider a turbulent flow bounded by two infinitely long and wide parallel walls. Here, x, y and z are denoted by the streamwise, wall-normal and spanwise direction, and the corresponding velocities are by u, v and w, respectively. The two walls are located at $y = -h$ and $y = h$, and they slide in opposite directions with speeds $u|_{y=-h} = -U_w$ and $u|_{y=h} = U_w$. A fundamental feature of the turbulent Couette flow is the mean-momentum balance, obtained by taking average of the streamwise momentum equation in time and two homogeneous directions:

$$\nu \frac{dU}{dy} - \overline{u'v'} = \frac{\tau_0}{\rho}, \tag{2.1}$$

where U is the mean velocity, $\overline{u'v'}$ the Reynolds shear stress (the overbar denotes the average in time and two homogeneous directions), τ_0 the applied shear stress, and ρ the density of the fluid. Here, we note that the validity of (2.1) is not limited only to the Couette flow – any parallel flow driven by a shear stress uniform in y should satisfy this equation. Therefore, (2.1) must be viewed as the generic mean-momentum equation for flows driven by a locally uniform shear stress.

Equation (2.1) provides some important physical insight into the velocity and length scales relevant to the present investigation. Since (2.1) is valid at every wall-normal location, the local shear flow can be viewed as the outcome of the applied local shear stress τ_0. This implies that the local velocity scale would be given from the local shear stress, such that: $u_\tau = \sqrt{\tau_0/\rho}$. We note that if the wall-normal location is chosen to be at the wall (i.e. $y = \pm h$), u_τ becomes identical to the friction velocity in the near-wall region. However, in the present case, u_τ also becomes the local velocity scale at every wall-normal location, as it originates from the constant shear stress τ_0 in the wall-normal direction. It is also important to note that (2.1) itself does not contain any description of the 'integral' length scale associated with the largest admissible eddies, and the scale of the largest eddies is here determined by the size of the computational domain. If the computational domain were sufficiently large horizontally, the relevant length scale of the largest admissible eddies would be given by the height of the channel. However, if the computational domain were artificially narrowed in the spanwise direction down to $O(\delta_\nu)$, as in a typical minimal channel simulation (Jiménez & Moin 1991; Hwang 2013), the size of the largest admissible eddies would be restricted to $O(\delta_\nu)$. In this case, the rate of turbulence dissipation would be given by $\mathcal{E} \sim u_\tau^3/\delta_\nu$, and the corresponding Kolmogorov length scale becomes identical to the viscous inner length scale: i.e. $\eta = \delta_\nu$. Normalising (2.1) with u_τ and η then leads to

$$\frac{dU^*}{dy^*} - \overline{u'v'}^* = 1, \tag{2.2}$$

where the superscript * indicates the resulting dimensionless variables. Here, we note that the use of the superscript *, instead of the commonly used $^+$ for normalisation by the viscous inner units, is to highlight that the assoicated velocity and length scales are relevant to the entire wall-normal location, including the outer and centreline region, where the use of the viscous inner scales would not usually make sense.

In (2.2), it is evident that the values of dU^*/dy^* and $\overline{u'v'}^*$ from a DNS with a sufficiently large horizonal computational domain would be strongly dependent upon the wall-normal location, as a range of different length scales would come into play at each of the wall-normal location – this can be easily checked by inspecting the available DNS database (see e.g. Pirozzoli *et al.* 2014). However, if the size of the eddies were

Simulation	Re	Re_τ	Δ_x^*	Δ_z^*	L_x^*	L_z^*	$N_x \times N_y \times N_z$	T_{avg}^*
LC1	10133	320	11.2	5.6	3355	112	$300 \times 261 \times 20$	48198
LC2	21333	488	10.7	5.4	3223	107	$300 \times 401 \times 20$	78066
LC3	33333	626	10.6	5.3	3195	107	$300 \times 497 \times 20$	77473
LC4	50000	814	11.4	5.7	3421	114	$300 \times 641 \times 20$	58363
SC1	10133	341	11.9	6.0	430	143	$36 \times 261 \times 24$	229623
SC2	21333	526	11.4	5.7	410	137	$36 \times 401 \times 24$	129517
SC3	33333	679	11.3	5.7	407	136	$36 \times 497 \times 24$	406020
SC4	50000	859	11.5	5.7	412	137	$36 \times 641 \times 24$	103292

TABLE 1. Simulation parameters in the present study (after dealiasing), and T_{avg}^* is the time interval for average. Here, in the name of simulations, the LC indicates 'long channel' and SC 'short channel' in the streamwise direction.

artificially restricted to the given Kolmogorov length scale, the velocity and length scales of the eddies at play would be uniquely given by u_τ and η. Therefore, dU^*/dy^* and $\overline{u'v'}^*$ are expected to be constant along the wall-normal direction, except the near-wall region where the no-slip boundary condition would break the homogeneity of (2.2). One such solution, but trivial, is given by $dU^*/dy^* = 1$ and $\overline{u'v'}^* = 0$. However, the presence of non-zero mean shear in the flow system considered here also suggests that there may exist other non-trivial solutions of (2.2) that involves non-zero Reynolds shear stress and the resulting turbulence production. The objective of the present study is essentially to address this point.

2.2. *Minimal Couette flow up to $Re_\tau \simeq 800$*

To seek the production mechanism at Kolmogorov microscale, a set of minimal-span direct numerical simulations ($L_z^* \simeq 100 - 140$) are performed. This approach, originally designed to investigate the self-sustaining nature of near-wall turbulence (e.g. Jiménez & Moin 1991; Hamilton *et al.* 1995; Hwang 2013), has recently been extended to study low-dimensional dynamics of the structures in the logarithmic and outer regions (Flores & Jiménez 2010; Hwang 2015; Hwang & Bengana 2016; de Giovanetti *et al.* 2016) as well as to assess the effect of wall-roughness with economical computational cost (Chung *et al.* 2015; MacDonald *et al.* 2017). The numerical solver used in this study is `diablo`, the detailed numerical method of which is well documented in Bewley (2014). In this solver, the streamwise and spanwise directions are discretised using Fourier series with 2/3 dealiasing rule, whereas the wall-normal direction is discretised using second-order central difference. The time integration is performed semi-implicitly based on the fractional-step method (Kim & Moin 1985). All the terms with wall-normal derivatives are implicitly advanced using second-order Crank-Nicolson method, while the rest of the terms are explicitly integrated using a third-order low-storage Runge-Kutta method. This solver has been verified through our previous studies (e.g. Hwang 2013).

Table 1 summarises the simulation parameters in the present study. The simulations are performed up to $Re = 50000$ ($Re \equiv U_w h/\nu$), and the corresponding friction Reynolds number is found to be $Re_\tau \simeq 800$ ($Re_\tau \equiv u_\tau h/\nu$). We note that this value of friction Reynolds number is much smaller than that expected from a simulation with a sufficiently large computational domain, as will be discuss in detail in §4.2. Both long and short streamwise computational domains are considered: the former with $L_x^* \simeq 3000$ is used to identify the full statistical features, while the latter with $L_x^* \simeq 400$

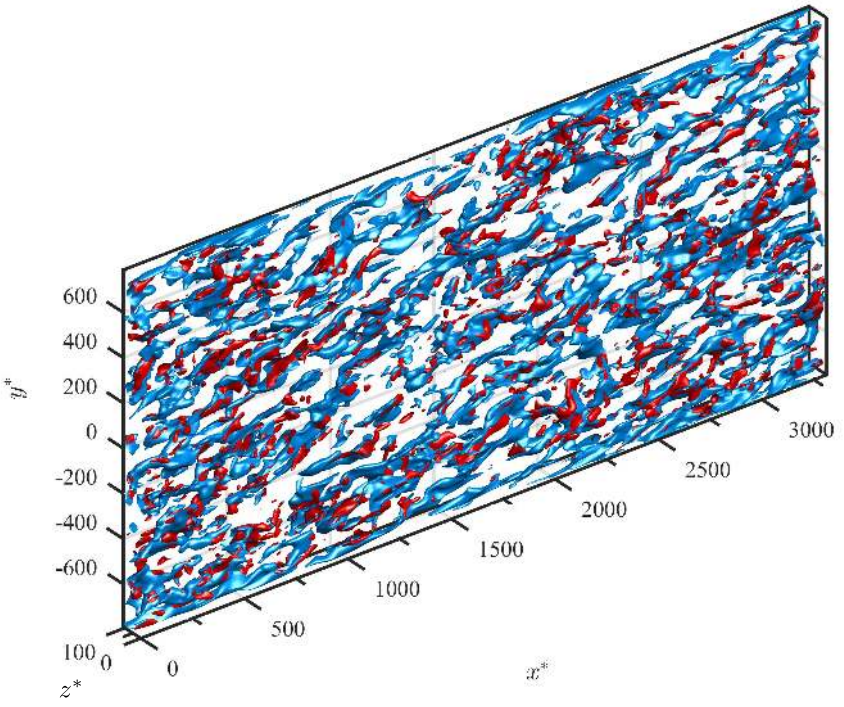

FIGURE 1. An instantaneous flow field of LC4 simulation. Here, the blue iso-surfaces indicate $u'^* = -2$, while the red ones are $v'^* = 1.5$.

is used to inspect the low-dimensional dynamics of the motions in the minimal spanwise domain. As was extensively discussed in Hwang (2013), numerical simulations with such a minimal spanwise domain contain a non-physical two-dimensional motion resolved by zero spanwise wavenumber (i.e. spanwise-independent cross-flow motion). This motion is essentially driven by the quasi two-dimensional nature of the present computational domain, and has been found to be dependent upon the size of the streamwise domain. This motion is therefore eliminated by adopting the filtering approach in Hwang (2013). Finally, it should be mentioned that the spanwise domain and the filtering of the two-dimensional motions here do not affect the mean-momentum balance in (2.2), as the equation for zero streamwise and spanwise wavenumbers in our numerical solver (i.e. the spatial mean equation) is not directly modified by them (see also figure 2*c*). Therefore, the time average of this equation with the spanwise-minimal domain and the removal of the spanwise independent cross-flow motion still yields the one identical to (2.2).

3. Results and discussion

3.1. *Turbulence statistics*

We first consider simulations with a long streamwise computational domain (i.e. LC simulations in table 1). Figure 1 is a visualisation of an instantaneous streamwise and wall-normal velocity field from the simulation performed at the highest Reynolds number (i.e. LC4). The flow field is occupied by small-scale eddies, the spanwise size of which just fits in the given spanwise computational domain. The motions associated with the streamwise velocity fluctuation (blue iso-surface in figure 1) tend to be elongated in the streamwise direction, but they are not very long. This feature becomes more evident if

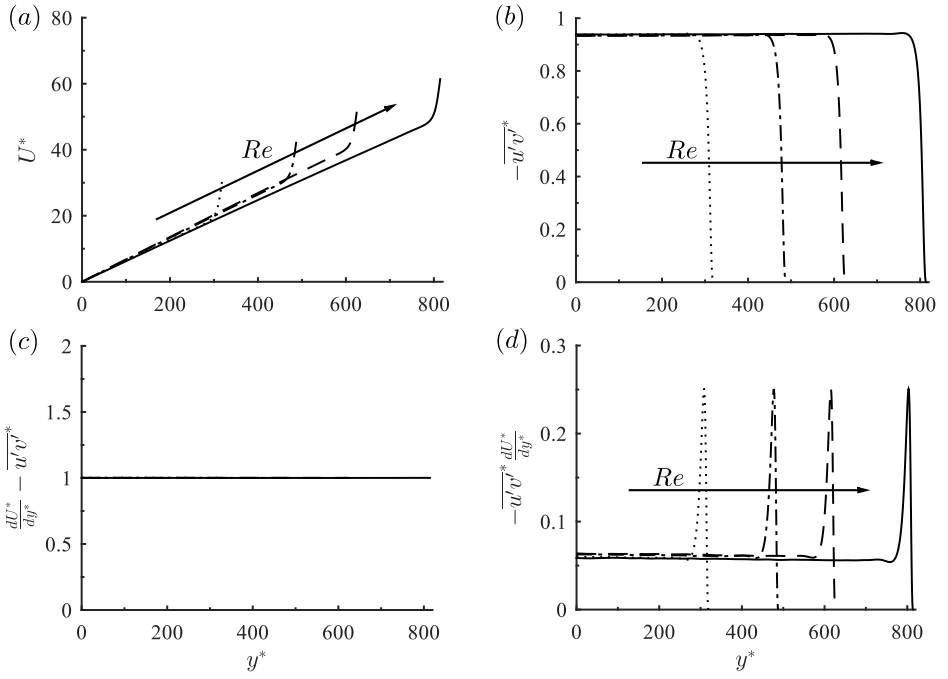

FIGURE 2. Turbulence statistics for mean-momentum balance and production: (*a*) $U^*(y^*)$; (*b*) $-\overline{u'v'}^*$; (*c*) $dU^*/dy^* - \overline{u'v'}^*$; (*d*) $-\overline{u'v'}^* dU^*/dy^*$. Here, ·····, LC1; –·–·–, LC2; - - - -, LC3; ———, LC4.

their streamwise extent is compared with that of the eddies in the near-wall region: the near-wall streamwise velocity fluctuation appears to be much longer than that in the bulk region of the flow. On the other hand, the streamwise extent of the wall-normal velocity fluctuations in the bulk region is slightly shorter than that for the streamwise velocity, and it does not seem to be greatly changed in the near-wall region (red iso-surface in figure 1).

Figure 2 shows turbulence statistics involved in construction of the mean-momentum balance and turbulence production. Here, the wall-normal coordinate in figure 2 is given by $y^* = y/\eta$, so that $y^* = 0$ corresponds to the centreline of the channel. This unconventional choice for the wall-normal coordinate is specifically to distinguish the Kolmogorov length scale η from the viscous inner length scale δ_ν. In the present study, we also show the statistics only for the upper half of the channel, as they are symmetric about $y^* = 0$. The mean velocity profile and the Reynolds shear stress for all the considered Reynolds numbers show impressively clear scaling with u_τ and η at all the wall-normal locations, except in the near-wall region where y^* is largest (figures 2*a*,*b*). In the bulk region, both the mean shear rate and the Reynolds shear stress are almost constant, being $dU^*/dy^* \simeq 0.07$ and $-\overline{u'v'}^* \simeq 0.93$. They also exactly satisfy the mean-momentum balance in (2.2) throughout the entire wall-normal location (figure 2*c*), demonstrating that the spanwise minimal domain and the filtering of the two-dimensional motions do not affect the mean-momentum balance (2.2). Finally, the constant values of the mean shear rate and the Reynolds shear stress at the Kolmogorov scale also imply a non-zero constant value of turbulence production given by $-\overline{u'v'}^* dU^*/dy^* \simeq 0.065$ (figure 2*d*). This evidently indicates that the turbulence production mechanism can indeed be active at the Kolmogorov microscale in the bulk region of the flow.

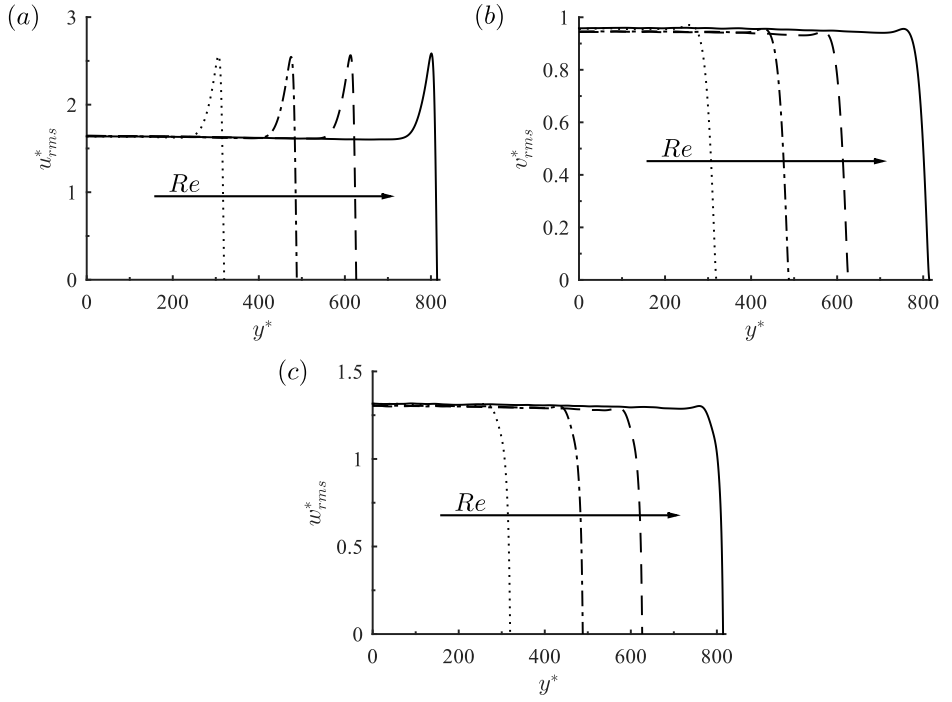

FIGURE 3. Turbulent velocity fluctuations: (*a*) $u^*_{rms}(y^*)$; (*b*) $v^*_{rms}(y^*)$; (*c*) $w^*_{rms}(y^*)$. Here, ·····, LC1; –·–·–, LC2; - - - -, LC3; ——, LC4.

The velocity fluctuations are shown in figure 3. As expected, all the turbulent velocity fluctuations exhibit very good scaling with u_τ and η over the entire wall-normal location, except the near-wall region. In the bulk region, the velocity fluctuations are found to be $u^*_{rms} \simeq 1.7$, $v^*_{rms} \simeq 0.93$ and $w^*_{rms} \simeq 1.3$. The different values of the velocity fluctuations suggest that the eddies populating the bulk are anisotropic, as one might expect given the presence of mean shear. In the near-wall region, the anisotropic nature of the velocity fluctuations becomes very strong: in particular, the magnitude of the near-wall streamwise velocity fluctuation is much larger than that in the bulk region; the other components vary only a little in the near-wall region before the drop in the viscous sub-layer. The near-wall velocity fluctuations are also found to scale very well in the wall-normal coordinate normalised by the viscous inner length scale (i.e. $y^+ = (y + h)/\delta_v$), consistent with the case of pressure-driven minimal turbulent channel (Hwang 2013). However, this issue does not exactly fall within the scope of the present study, and the related discussion is given in Appendix A.

One-dimensional spectra also exhibit essentially uniform statistics in the bulk region. Figure 4 shows the spanwise and streamwise wavenumber spectra of streamwise, wall-normal, spanwise velocities and Reynolds shear stress from the lowest and the highest Reynolds numbers (LC1 and LC4). All the spectra in figure 4 exhibit remarkably good scaling with u_τ and η, while being constant at all the wall-normal locations except the near-wall region. The peaks in the spanwise wavenumber spectra of all the variables (figures 4*a*,*c*,*e*,*g*) appear at the largest spanwise wavelength, indicating that the spanwise size of the motions at all the wall-normal locations in the flow field is restricted by the narrow spanwise computational domain (note that the motions uniform in the spanwise direction are eliminated in the simulations, as discussed in §2.2). The

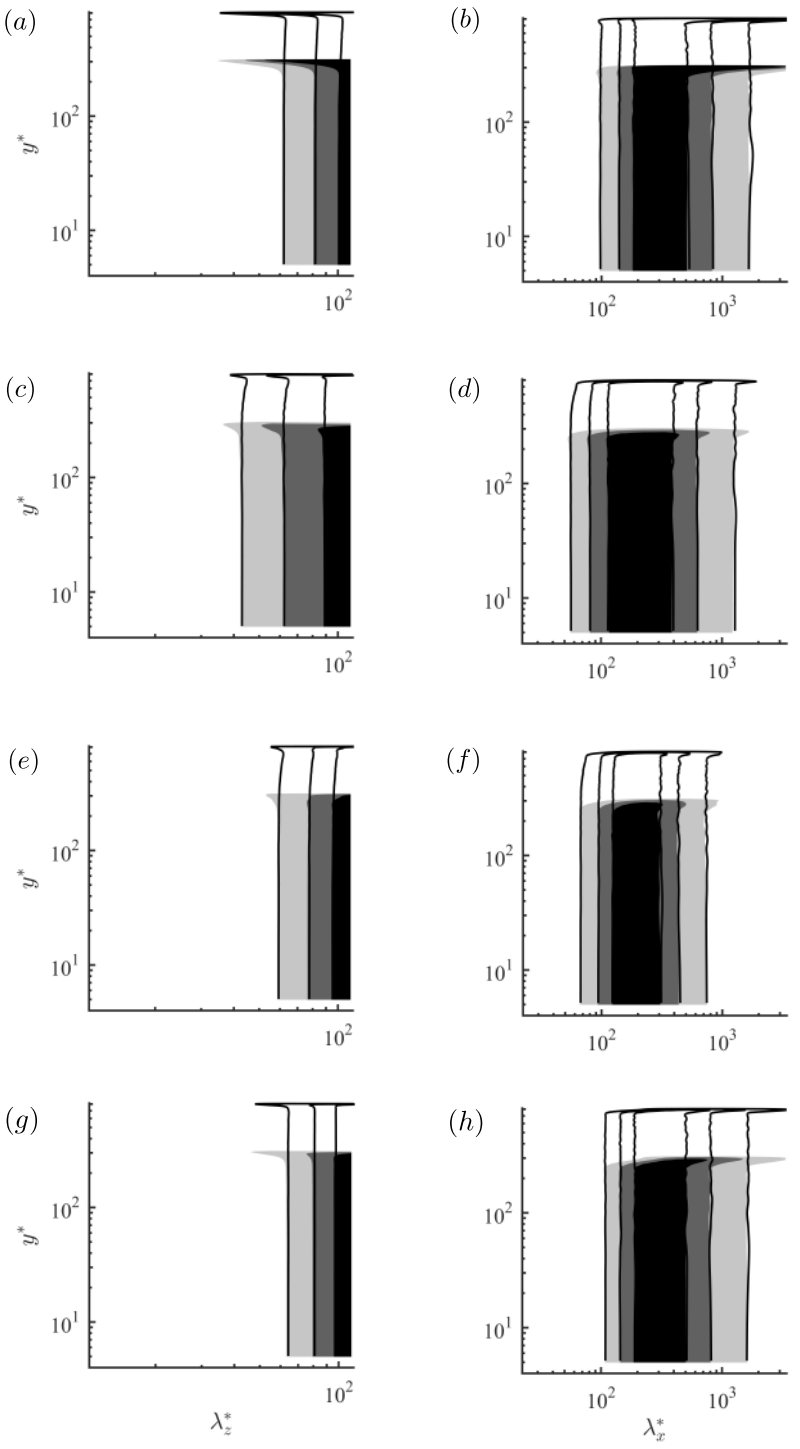

FIGURE 4. One-dimensional pre-multiplied (a, c, e, g) spanwise and (b, d, f, h) streamwise wavenumber spectra of (a, b) streamwise velocity, (c, d) wall-normal velocity, (e, f) spanwise velocity and (g, h) Reynolds stress. Here: shaded, LC1; solid, LC4. In (a, b), the contour levels are 0.125, 0.25 and 0.375 times of each of the maximum, while in $(c - h)$, they are 0.25, 0.5 and 0.75 times of each of the maximum.

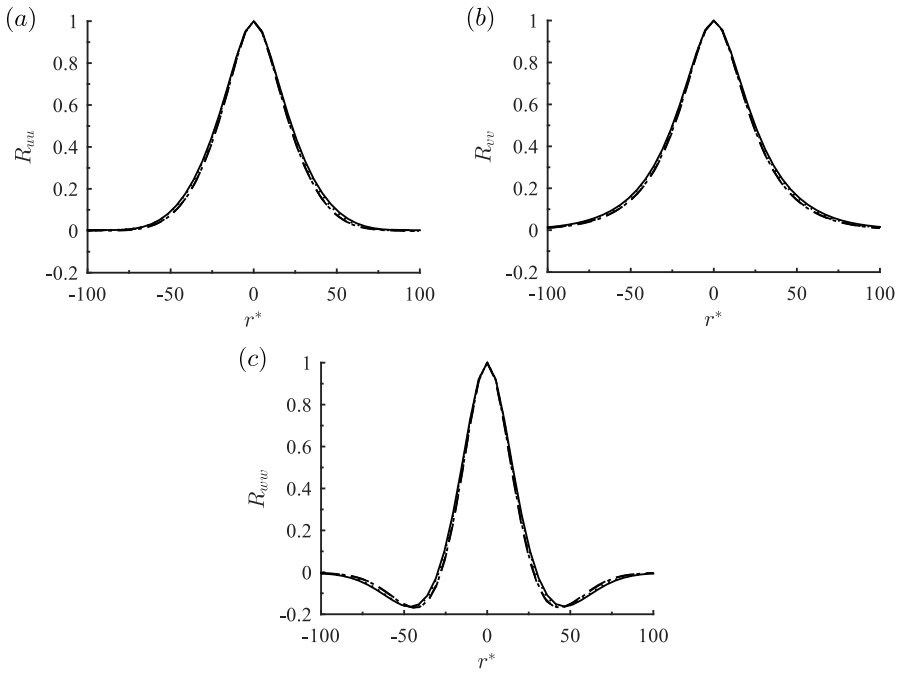

FIGURE 5. The wall-normal correlation functions with the reference point at $y_{\mathrm{ref}} = 0$: (a) $R_{uu}(r^*;0)$; (b) $R_{vv}(r^*;0)$; (c) $R_{ww}(r^*;0)$. Here, ·····, LC1; —·—·—, LC2; - - - -, LC3; ———, LC4.

streamwise wavenumber spectra are also shown to indicate the streamwise length scale of the structures in the bulk region. The streamwise extent of the streamwise velocity structure is characterised by $\lambda_x^* \simeq 300$ (figure 4*b*), whereas that of the wall-normal and spanwise velocity structures is $\lambda_x^* \simeq 200$ (figures 4*d*,*f*). The streamwise length scale of the Reynolds shear stress is rather similar to that of the streamwise velocity spectra, revealing the peak at $\lambda_x^* \simeq 300$ (figure 4*h*). The spectra in the near-wall region are much more anisotropic than those in the bulk region, and their peaks generally appear at larger streamwise wavelengths. The overall features of the spectra in the near-wall region are almost identical to those observed in the spanwise minimal unit of pressure-driven channel flow (Hwang 2013), as discussed in Appendix A (see also figure 14).

Figure 1 clearly shows that the wall-normal size of the eddies in the bulk region is not very large, which follows from the fact that all the turbulence statistics are constant in the wall-normal direction (figures 2-4). Therefore, to characterise the wall-normal size of the eddies, two-point correlation function in the wall-normal direction is introduced. For example, the correlation function for the streamwise velocity is given by

$$R_{uu}(r;y_{\mathrm{ref}}) = \frac{\overline{u'(y_{\mathrm{ref}}+r)u'(y_{\mathrm{ref}})}}{\overline{u'(y_{\mathrm{ref}})u'(y_{\mathrm{ref}})}}, \tag{3.1}$$

where y_{ref} is the reference point. Similarly, the correlation functions for the wall-normal and spanwise velocities are computed, and they are denoted by $R_{vv}(r;y_{\mathrm{ref}})$ and $R_{ww}(r;y_{\mathrm{ref}})$, respectively.

The computed correlation functions with $y_{\mathrm{ref}} = 0$ (i.e. the centre of the channel) is shown in figure 5 at all the Reynolds numbers considered. All the computed correlation functions for each velocity component are almost identical when they are scaled with the

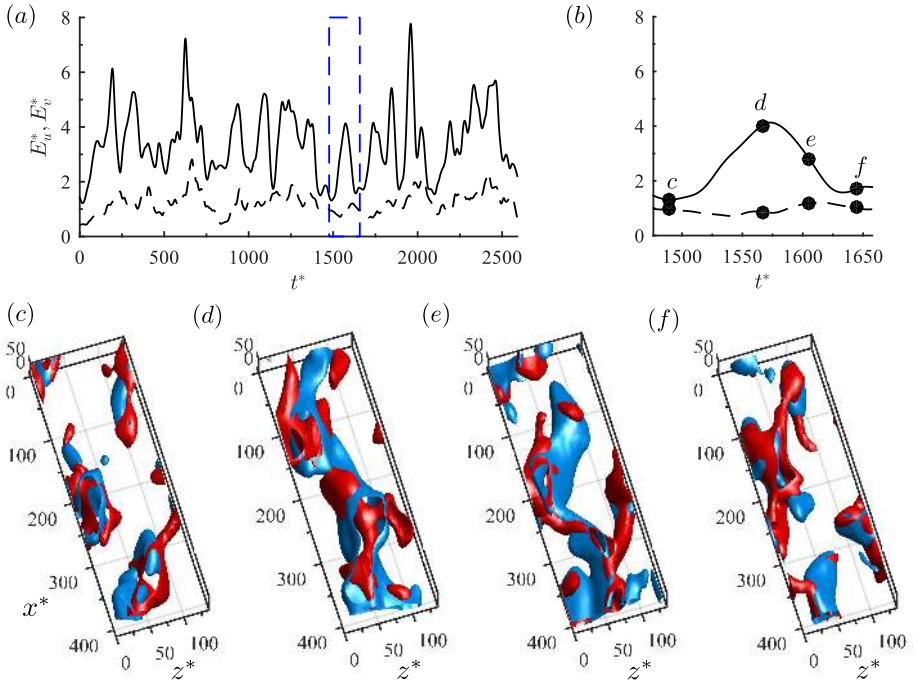

FIGURE 6. Temporal evolution of flow field in the core region ($0 \leqslant y^* \leqslant 50$) from SC2 simulation: (a) time trace of E_u^* (solid) and E_v^* (dashed); (b) magnification of (a) for $t^* \in [1476, 1658]$; $(c-f)$ the corresponding flow visualisation. In $(c-f)$, the red and blue iso surfaces indicate $u'^* = -1.2$ and $v'^* = 0.8$, respectively.

Kolmogorov length scale η. Their tails are found to reach zero roughly at $r^* \simeq \pm 50 \sim \pm 100$, indicating that the wall-normal size of the eddies would be $l^* \simeq 50 \sim 100$. This also implies that the constant turbulence statistics in the bulk region of the flow along the wall-normal direction (figures 2-4) are due to the homogeneous distribution of the statistically and dynamically identical eddies at the Kolmogorov scale at all wall-normal locations except the near wall. In this respect, it should be mentioned that any solutions of the Navier–Stokes equation with uniform shear flow would be invariant under the wall-normal translation, as long as the solutions are not affected by the boundary condition that would break the invariance (e.g. no-slip condition). It is evident that the eddies in the bulk region of the present numerical simulations belong to this case, and the only expected difference between the eddies at different wall-normal locations should therefore be their mean streamwise advection velocity.

3.2. *Self-sustained structures at the Kolmogorov scale*

Now, to study low-dimensional dynamics of the motions in the bulk region, we consider a much shorter streamwise computational box size (SC cases in table 1). Particular emphasis of this section is given to find any links between the dynamics of the eddies in the bulk region and the SSP/VWI. Instantaneous flow fields around $y^* = 0$ are first inspected while tracking turbulent kinetic energy of each velocity component obtained

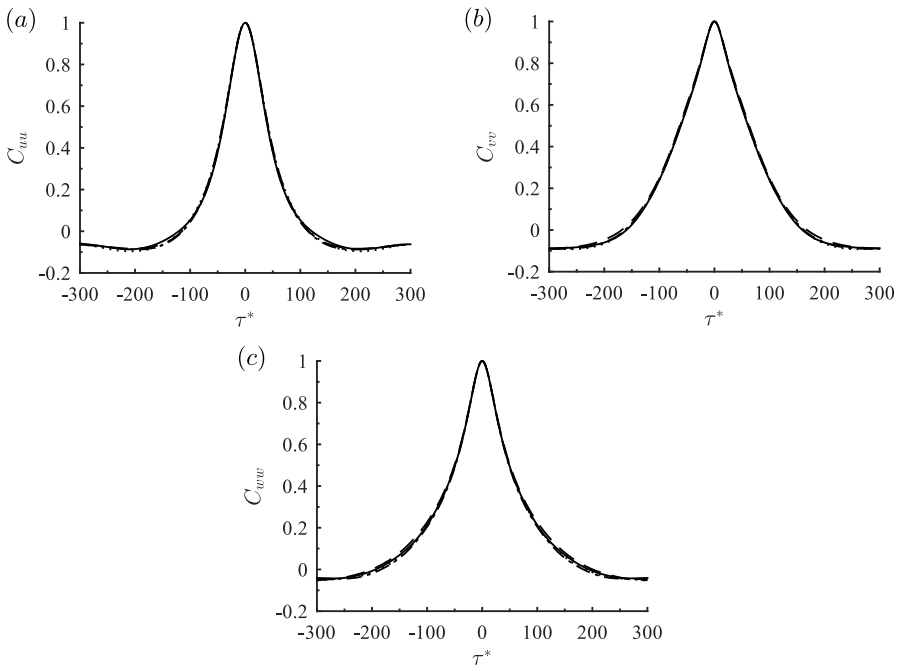

FIGURE 7. Temporal autocorrelation: (a) $C_{uu}(\tau^*)$; (b) $C_{vv}(\tau^*)$; and (c) $C_{ww}(\tau^*)$. Here, ·····, SC1; —·—·—, SC2; - - - -, SC3; ———, SC4. Note that all the correlation functions are almost identical when normalised by Kolmogorov scales.

by averaging over a small domain around the centreline: i.e.

$$E_u^* = \frac{1}{V^*}\int_{\Omega^*} u^{*2}\, dV, \quad E_v^* = \frac{1}{V^*}\int_{\Omega^*} v^{*2}\, dV, \quad E_w^* = \frac{1}{V^*}\int_{\Omega^*} w^{*2}\, dV, \tag{3.2}$$

where $\Omega^* = [0, L_x^*] \times [0, l_y^*] \times [0, L_z^*]$ with $l_y^* = 50$ and V^* is the volume of Ω^*. Here, we note that the size of Ω^* is chosen to be just enough for a single eddy at the Kolmogorov length scale (see also the wall-normal autocorrelation in figure 5).

Figure 6 shows the temporal evolution of E_u^* and E_v^* and the corresponding flow visualisation in the region Ω^*. Since E_v^* and E_w^* have been found to show strong correlation (see figure 11*d*), E_w^* is not shown here for brevity. Both E_u^* and E_v^* show temporal oscillations with a time scale of $T^* \simeq 200 \sim 300$ (figure 6*a*), and occur with some phase difference. Although the flow fields are fairly chaotic in general and the structures are also found to often move up and down across the wall-normal boundary of Ω^*, a careful observation leads us to conclude that the overall behaviour of the flow fields is quite similar to the SSP/VWI observed in Hamilton *et al.* (1995). The strong wall-normal velocity structures (figure 6*c*) are transformed into a highly amplified and elongated streamwise velocity structure, reminiscent of a 'streak' (figure 6*d*). The amplified streamwise velocity structure meanders along the streamwise direction (figure 6*e*), and eventually breaks down with regeneration of the wall-normal velocity structures (figure 6*f*). This process occurs in a cyclic manner, detailed later with respect to figure 11.

The eddy turn-over dynamics observed in figure 6 is also found to scale very well with the Kolmogorov microscale. This is shown by computing correlation functions with the

Simulation	Re	Re_τ	Δ_x^*	Δ_z^*	L_x^*	L_z^*	$N_x \times N_y \times N_z$	δ^*	T_{avg}^*
FSC2	21333	176	9.6	5.0	423	141	$44 \times 401 \times 28$	70	131315

TABLE 2. Simulation parameters for the numerical experiment that removes all the structures except the core region (after dealiasing). Here, T_{avg}^* is the time interval for average and the definition of δ^* is given in (3.4).

variables defined in (3.2):

$$C_{ij}(\tau) = \frac{\langle E_i^*(t+\tau) E_j^*(t) \rangle}{\sqrt{\langle {E_i^*}^2(t) \rangle} \sqrt{\langle {E_j^*}^2(t) \rangle}}, \tag{3.3}$$

where $i, j = u, v, w$ and $\langle \cdot \rangle$ indicates average in time. Figure 7 shows the autocorrelations computed for all the Reynolds numbers. They are indeed almost indistinguishable when scaled by u_τ^* and η. The autocorrelation functions of all the variables reach zero at $t^* \simeq \pm 100 \sim \pm 150$, suggesting that the time scale of the eddy turn-over dynamics in figure 6 would be $T^* \simeq 200 \sim 300$. Interestingly, this time scale is almost identical to that of the self-sustaining process in near-wall turbulence (e.g. Jiménez *et al.* 2005) (see also §4.1 for further discussion).

The visual inspection of a series of flow fields suggests that the eddies at Kolmogorov scale in the bulk region of the flow appear to bear the SSP/VWI mechanism. It is important to mention that given fluid motions, the dynamics of which is governed by the SSP/VWI mechanism, should be able to sustain themselves in the absence of other motions (e.g. Jiménez & Pinelli 1999; Hwang & Cossu 2010; Hwang 2015). Therefore, to provide more solid evidence on the existence of the SSP/VWI mechanism, we design a numerical experiment which removes all the motions except the ones in the core region. The removal has been performed by applying a damping technique similar to the one described in Jiménez & Simens (2001). At each Runge-Kutta substep for the time integration, the right-hand side of the discretised momentum equation, denoted by RHS, is multiplied by a damping function $\mu(y)$: i.e.

$$\widehat{\mathrm{RHS}}(y; k_x, k_z) \;\rightarrow\; \mu(y) \widehat{\mathrm{RHS}}(y; k_x, k_z), \tag{3.4a}$$

where $\widehat{\cdot}$ denotes the Fourier-transformed state, and k_x and k_z are the streamwise and spanwise wavenumbers, respectively. The damping function $\mu(y)$ is chosen as

$$\mu(y) = \begin{cases} \mu_0 & \text{for } |y^*| \geqslant \delta^*, \\ 1 & \text{for } |y^*| < \delta^*, \end{cases} \tag{3.4b}$$

where the damping factor μ_0 provides removal of the motions at $|y^*| \geqslant \delta^*$ if $\mu_0 < 1$. Several different values of μ_0 have been tested, and, in the present study, we have chosen $\mu_0 = 0.9$ which provides a marginal damping just enough to remove the target structures. Finally, it should be mentioned that the damping technique (3.4) is not applied to the mean component for $k_x = 0$ and $k_z = 0$ to maintain the mean-momentum balance (2.2) (see also figure 9*c*).

The removal of the structures except the core region is performed by gradually decreasing δ^* to a value at which turbulence in the core region is only just sustained. Table 2 summarises simulation parameters of this numerical experiment. Here, the aspect ratio of the computational domain is kept to be $L_x/L_z = 3$. Figure 8 are visualisations

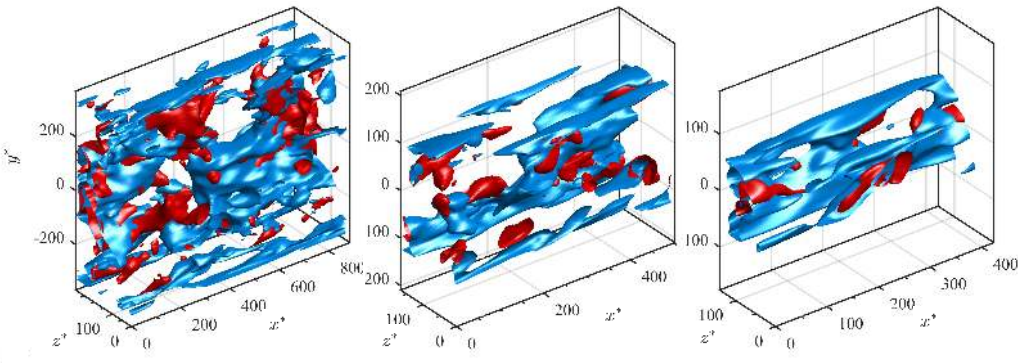

FIGURE 8. Instantaneous flow fields of FSC2 simulation with different damping height: (a) $\delta^* = 333$; (b) $\delta^* = 126$; (c) $\delta^* = 70$. Here, the blue iso-surfaces indicate $u'^* = -2$, while the red ones are $v'^* = 1.5$.

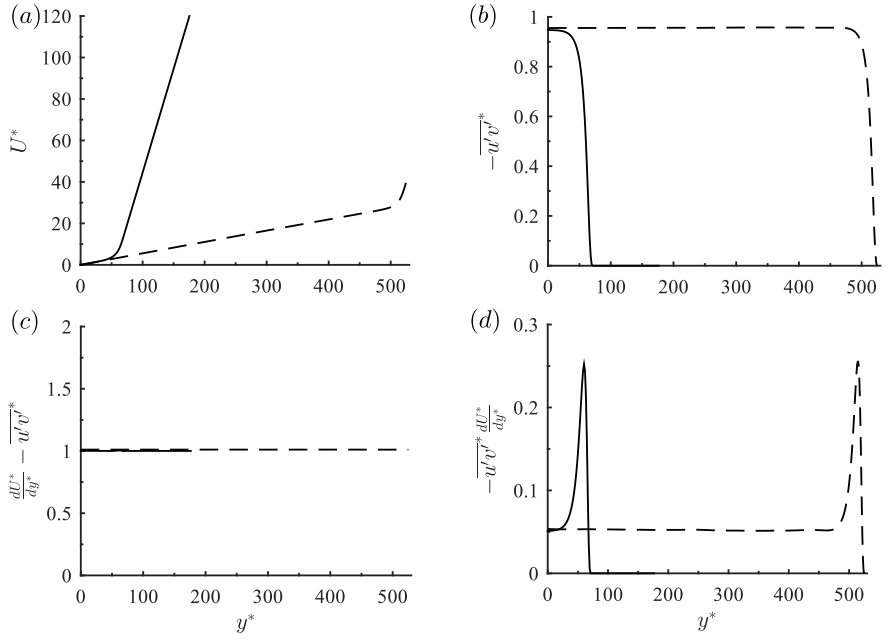

FIGURE 9. Turbulence statistics for mean-momentum balance and production: (*a*) $U^*(y^*)$; (*b*) $-\overline{u'v'}^*$; (*c*) $dU^*/dy^* - \overline{u'v'}^*$; (*d*) $-\overline{u'v'}^* dU^*/dy^*$. Here, - - - -, SC2; ——, FSC2.

of the remaining turbulent structures for three different δ^* values. The smallest possible δ^* that maintains turbulence in the core region is found to be $\delta^* \simeq 70$. We note that this value is consistent with the wall-normal autocorrelation in figure 5 where the correlation functions reach zero at $y^* \simeq 50 - 100$, indicating that the core-region structures, the size of which is $O(100\eta)$, sustain themselves.

Turbulence statistics for mean-momentum balance and production from the simulation only with the self-sustaining core structures (FSC2) are compared with those of a minimal channel simulation in figure 9. Despite the harsh nature of the applied damping (3.4), the mean shear rate, Reynolds shear stress and turbulence production in the core region ($y^* < 30 \sim 40$) of the FSC2 simulation still show reasonably good agreement with

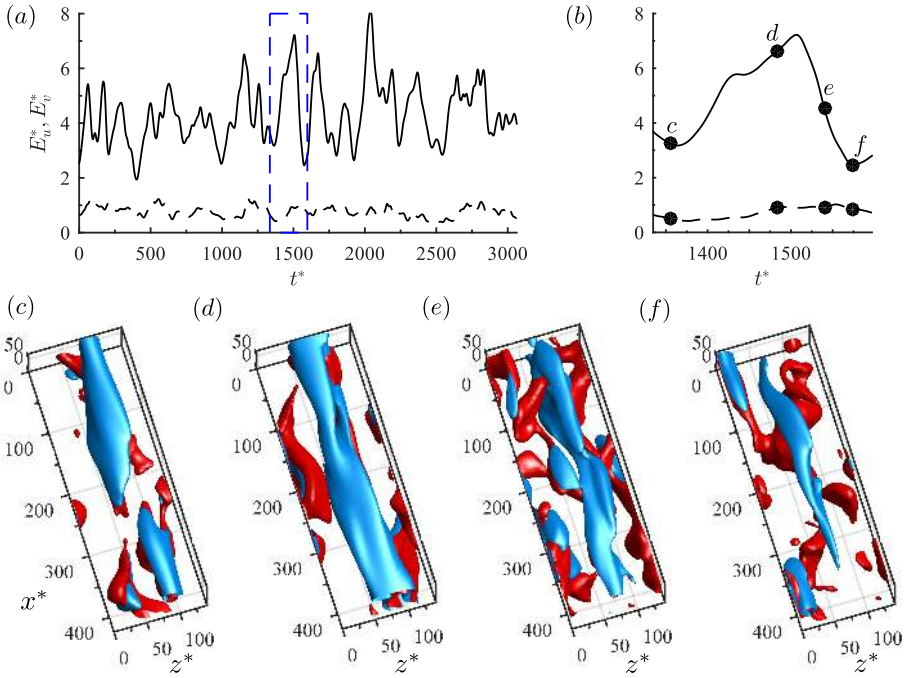

FIGURE 10. Temporal evolution of flow field in the core region ($0 \leqslant y^* \leqslant 70$) from FSC2 simulation: (a) time trace of E_u^* (solid) and E_v^* (dashed); (b) magnification of (a) for $t^* \in [1335, 1597]$; $(c-f)$ the corresponding flow visualisation. In $(c-f)$, the red and blue iso surfaces indicate $u'^* = -2.5$ and $v'^* = 0.8$, respectively.

those of the full minimal channel simulation. This suggests that the dynamics of the structures in the core region is not significantly disrupted by damping of the structures at $|y^*| > 70$. Application of the damping (3.4) is also found to make the mean shear rate dU^*/dy^* rapidly change for $50 \lesssim y^* \lesssim 70$ (figure 9*a*) where the Reynolds shear stress rapidly decays (figure 9*b*) to satisfy the mean-momentum balance (2.2) (figure 9*c*). In this location, turbulence production also exhibits a large peak (figure 9*d*), and, interestingly, its peak value appears to be remarkably similar to what is observed in the near-wall region where the Reynolds shear stress also decays rapidly due to the no-slip boundary condition (see the dashed line in figure 9*d* around $y^* \simeq 500$). A detailed discussion on this observation will be given in §4.1.

Temporal evolution of the flow structures in FSC2 simulation is shown in figure 10. The time trace of E_u^* and E_v^* in FSC2 simulation also exhibits temporal oscillations, and their time scale appears to be roughly at $T^* \simeq 200 \sim 300$, not very different from that observed in figure 6 (figure 10*a*). The temporal oscillations of E_u^* and E_v^* also show a phase difference (figure 10*b*). Visualisation of the instantaneous flow fields along the different phase in a single oscillation period reveals that the motions in FSC2 simulation also seem to undergo the SSP/VWI, similarly to the observation made in figure 6. The strong wall-normal velocity structures (figure 10*c*) highly amplify a streaky structure (figure 10*d*). The amplified streak subsequently meanders along the streamwise direction (figure 10*e*), resulting in its breakdown with regeneration of the wall-normal velocity structure (figure 10*f*).

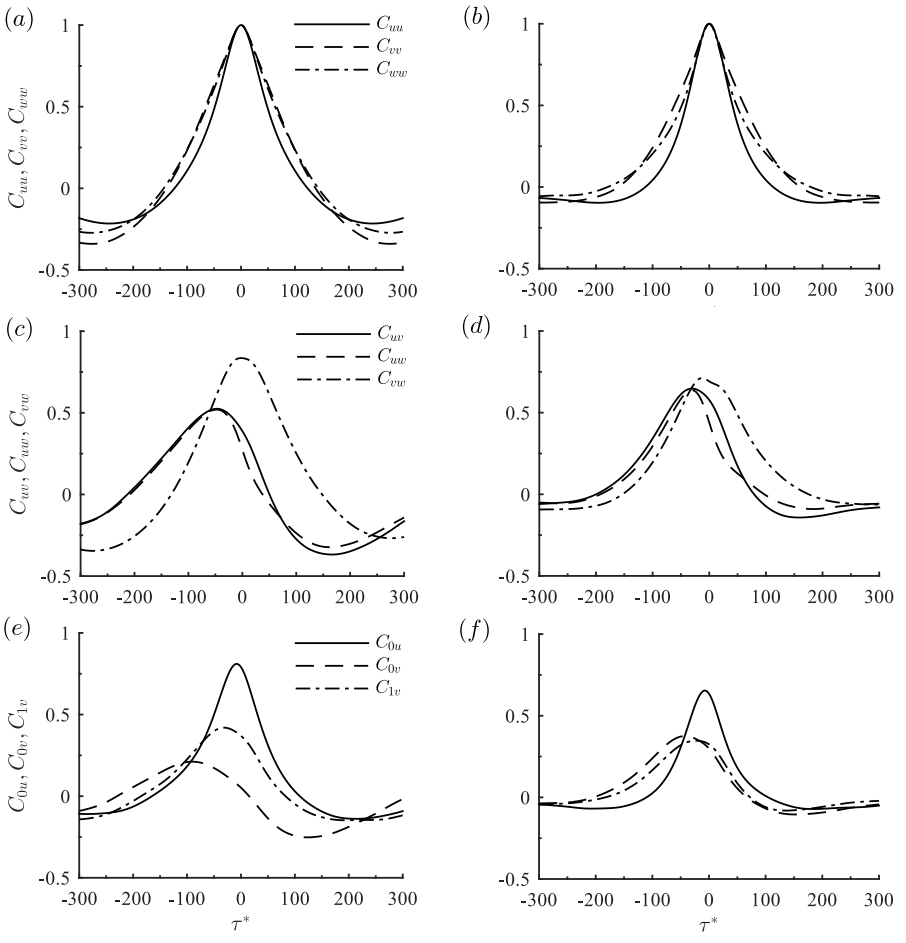

FIGURE 11. Comparison of auto- and cross-correlation functions from (a, c, e) FSC2 and (b, d, f) SC2 simulations: (a, b) C_{uu}, C_{vv}, C_{ww}; (c, d) C_{uv}, C_{uw}, C_{vw}; (e, f) C_{0u}, C_{0v}, C_{1v}.

To make more quantitative comparison between the dynamics of FSC2 and SC2 simulations, auto- and cross-correlations of the time-dependent variables such as those defined in (3.2) are examined as in e.g. Hwang & Bengana (2016). Here, we also introduce two additional variables:

$$E_0^* = \frac{1}{l_y^*} \int_0^{l_y^*} \left(|\hat{u}^*(y; k_x, k_z)|^2 + |\hat{v}^*(y; k_x, k_z)|^2 + |\hat{w}^*(y; k_x, k_z)|^2 \right) \mathrm{d}y, \tag{3.5a}$$

for $k_x = 0$ and $k_z = 2\pi/L_z$, and

$$E_1^* = \frac{1}{l_y^*} \int_0^{l_y^*} \left(|\hat{u}^*(y; k_x, k_z)|^2 + |\hat{v}^*(y; k_x, k_z)|^2 + |\hat{w}^*(y; k_x, k_z)|^2 \right) \mathrm{d}y, \tag{3.5b}$$

for $k_x = 2\pi/L_x$ and $k_z = 2\pi/L_z$, where E_0^* represents energy of the elongated motion extending over the entire streamwise domain, while E_1^* measures the strength of wavy meandering motion (i.e. streak instability). The cross-correlation functions are subsequently computed following the definition in (3.3).

Figure 11 compares a number of different auto- and cross-correlations computed from FSC2 with those from SC2 simulation. The auto-correlations from both FSC2 (figure 11*a*)

and SC2 simulation (figure 11*b*) show their tails reaching zero at $\tau^* \simeq \pm 100 \sim \pm 150$, indicating that the turn-over time scale of the structures in both of the cases would be $T^* \simeq 200 \sim 300$, consistent with the observations in figures 6 and 10. The cross-correlations between E_u^*, E_v^* and E_w^* of both cases (figures 11*c*,*d*) reveal that the wall-normal and spanwise velocities are well correlated to each other, indicating the presence of the streamwise roll-like structures (C_{vw} in figures 11*c*,*d*). On the other hand, E_v^* and E_w^* exhibit phase difference from E_u^*: the peaks of C_{uv} and C_{uw} in both of the cases appear at $\tau^* \simeq -60 \sim -40$. The cross-correlations of E_u^* with E_0^* in both of the cases (C_{0u} in figures 11*e*,*f*) show a large value around $\tau^* \simeq 0$. This implies that E_u^* represents the elongated motion of the streamwise velocity, indicating the streaky motion in figures 6 and 10. For this reason, the cross-correlation between E_0^* and E_v^* in both cases (C_{0v} in figures 11*e*,*f*) exhibits a peak at $\tau^* \simeq -80 \sim -50$, similarly to C_{uv}. Finally, the cross-correlation between E_1^* and E_v^* in both cases (C_{1v} in figures 11*e*,*f*) reveals its peak location around $\tau^* \simeq -40 \sim -20$. This indicates that a streamwise meandering motion consistently appears before the streamwise roll-like structures are generated.

Overall, the auto- and cross-correlations from FSC2 and SC2 simulations show qualitatively good agreement with each other, suggesting that the dynamics of the self-sustaining structures in the FSC2 case is not very different from that in the SC2 case. Furthermore, the correlations also suggest that there exists a statistically cyclic process in the core region of both simulations, which occurs in the following order:

$$E_u^* \;\&\; E_0^* \;\longrightarrow\; E_1^* \;\longrightarrow\; E_v^* \;\&\; E_w^* \;\longrightarrow\; E_u^* \;\&\; E_0^*, \tag{3.6}$$

with the turn-over time scale, $T^* \simeq 200 \sim 300$. The fluid motion associated with E_u^* and E_0^* indicate an elongated streamwise velocity structure, very likely to be a 'streak', and E_1^* indicate its streak meandering motion presumably caused by a streak instability. The streak instability process occurs before generation of streamwise roll-like structures represented by E_v^* and E_w^*. The statistical evidence in figure 11 therefore firmly indicates the existence of the SSP/VWI in the core region of the SC2 simulation. Here, it should be stressed that the existence of the SSP/VWI in the SC2 simulation is not limited only to the core region. The observed dynamics in the core region should be invariant under the wall-normal translation, thus it has to be relevant to other wall-normal locations, except the near-wall region where the translational invariance would be broken due to the no-slip boundary condition. However, also in the near-wall region, it is well understood that the SSP/VWI is the main driving mechanism of turbulence (Jiménez & Moin 1991; Jiménez & Pinelli 1999). In summary, we conclude that the SSP/VWI is the dominant mechanism of turbulence production at all wall-normal locations in the present minimal-span simulations.

4. Discussion

An important outcome of the present minimal-span numerical simulations for turbulent Couette flow is that they enable us to generate a uniform shear flow in the bulk turbulent region, unaffected by the wall region. In particular, the minimal-span simulations enable us to isolate and discuss processes at the Kolmogorov scale in the bulk. We have shown that there indeed exists a turbulence production mechanism at the Kolmogorov microscale in the bulk region of turbulent Couette flow. The related eddies essentially originate from the mean shear existing at every wall-normal location, and do not rely on the presence of the wall. In this respect, the present study is consistent with Mizuno & Jiménez (2013), where a scaling procedure is used to eliminate wall effects. Statistical evidence also firmly indicates that the turbulence production mechanism is supported

by the SSP/VWI. This suggests that the self-similar invariant solutions found by the recent studies (Blackburn *et al.* 2013; Deguchi 2015; Eckhardt & Zammert 2016) may be relevant to turbulence production observed in the present study.

It is yet to be clarified whether the eddies observed in the present study may be associated with the turbulent cascade. We note that the eddies involved in the energy cascade, and dissipation of a typical turbulent flow at high Reynolds numbers, are expected to be 'driven' by the energy transferred from 'large scale' due to the balance between turbulence production and dissipation (Kolmogorov 1941, 1991). However, the eddies in the present minimal-span simulation emerge in the absence of any large scales by taking energy directly from the mean shear. Further, the Kolmogorov-scale eddies in the present study are not isotropic, unlike the hypothesis of Kolmogorov (1941, 1991), although the hypothesis itself may not be fully justified yet. Finally, it is important to point out that the self-sustaining eddies in the present study are still much larger than those associated with turbulence dissipation, even though their size scales with the Kolmogorov microscale. Indeed, the typical size of the dissipative eddies at the Kolmogorov scale is only $O(\eta)$ (Jiménez & Wray 1998), much smaller than the eddies in the present study at $O(100\eta)$.

Taking these observations together, the self-sustaining eddies at the Kolmogorov microscale observed in the present study are unlikely to be relevant for full-scale turbulent flows at high Reynolds number. Instead, these eddies are more relevant for flow at transitional Reynolds numbers in the presence of uniform shear: the small size of the eddies at $O(100\eta)$, originating from artificial restriction of the spanwise length scale by the periodic boundary condition, reduces the characteristic Reynolds number to be $Re_c(\equiv u_\tau(100\eta)/\nu) = 100$, resulting in a transitional flow where there is little separation between the length scales of turbulence production and dissipation. We note that the same appears to be true for turbulence in the near-wall region (i.e. buffer layer): the length scale of turbulence production is artificially restricted by the distance from the wall due to the no-slip boundary condition, and the smallest possible length scale of turbulence would therefore be given by the balance between the associated production and viscous dissipation. This explains why the viscous inner length scale is the same as the near-wall Kolmogorov length scale. The present study implies that such a phenomenon may occur whenever the size of the eddies is artificially restricted e.g. by a boundary condition.

4.1. *Uniform shear vs near-wall turbulence*

Uniform shear turbulence has often been compared with near-wall turbulence (Lee *et al.* 1990; Sekimoto *et al.* 2016). Here we are able to make a direct comparison between them, while maintaining all the other conditions, such as applied shear stress and horizontal boundary conditions, to be exactly the same. In the present study, we have shown that the eddies in the bulk region are generated by the same mechanism as in near-wall turbulence, i.e. the SSP/VWI (figures 6) (Hamilton *et al.* 1995; Jiménez & Pinelli 1999; Schoppa & Hussain 2002). The eddy turn-over time scale of the bulk region is also found to be $T^* \simeq 200 - 300$ at least with $L_x^* \simeq 400$ (figure 7), and this value corresponds very well to the typical near-wall time scale $T^+ \simeq 200 - 300$ (Jiménez *et al.* 2005). However, the near-wall turbulence appears to be more anisotropic than uniform shear turbulence (figures 3 and 4): in particular, the streamwise turbulence intensity of near-wall turbulence is much stronger than that for the uniform shear case (figure 3), and the related streaky structures also appear to be twice as elongated in the streamwise direction (figures 4 and 14). This implies that the dynamics of coherent structures in near-wall turbulence is very similar to that in uniform shear turbulence, but their statistical features are significantly different.

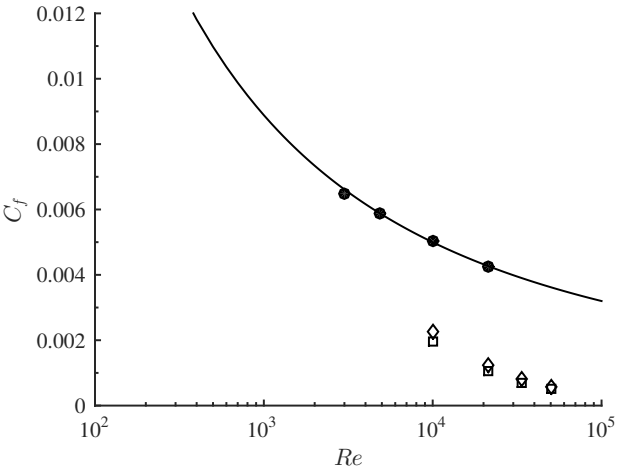

FIGURE 12. Variation of skin-friction coefficient with Re: ———, empirical fit by Robertson (1959), $C_f = 0.424(\ln Re)^{-2}$; •, DNS by Pirozzoli *et al.* (2014); □, LC cases; ◇, SC cases.

One such important statistical difference is the large value of production in the near-wall turbulence, the peak value of which is about four to five times greater than that of uniform shear turbulence (figure 2*d*). In fact, this is a very common feature of the near-wall region in any simulation of wall-bounded shear flows, and, for many years, it has led to a misunderstanding that the near-wall region is the most vigorous location where turbulence production is dominated (see also Marusic *et al.* 2010, for a further discussion). However, the numerical experiments in the present study suggest that the emergence of such a peak in the near-wall turbulence production may be a local 'transitional' effect simply caused by no-slip boundary condition. In the near-wall region of the present minimal-span simulation, the no-slip condition leads $-\overline{u'v'}^*$ to decay rapidly on approaching to the wall (figure 2*b*). Since the mean-momentum balance (2.2) needs to be always satisfied, this results in a rapid increase of dU^*/dy^* in the near-wall region. Here, we note that the value of $-\overline{u'v'}^* dU^*/dy^*$ subject to (2.2) mathematically reaches its maximum when $dU^*/dy^* = -\overline{u'v'}^* = 0.5$. Since $-\overline{u'v'}^* \simeq 0.93$ in the bulk region, the only place where $-\overline{u'v'}^* = 0.5$ is physically possible would be the near-wall region, where the maximum of $-\overline{u'v'}^* dU^*/dy^*$ indeed emerges at $y^+ \simeq 10$ in the present minimal-span simulations (see also figure 14*a*). It is important to mention that the same phenomenon also occurs in the FSC2 simulation where all the structures are artificially damped out except those in the core region. In the FSC2 simulation, the location of $-\overline{u'v'}^* = 0.5$ is given by $|y^*| \simeq 60$ due to the applied artificial damping (figure 9*b*), and $-\overline{u'v'}^* dU^*/dy^*$ reaches the maximum at this location. This implies that the emergence of the large peak of $-\overline{u'v'}^* dU^*/dy^*$ in both of the SC2 and FSC2 simulations is essentially due to the decaying Reynolds shear stress subject to (2.2), indicating that the large value of production in the near-wall turbulence may be a local effect caused by the no-slip boundary condition.

It should also be stressed that this feature is not necessarily limited to the present minimal-span simulations of turbulent Couette flow – it appears to be generic, at least for any parallel internal wall-bounded shear flows. For example, the mean-momentum

balance in a pressure-driven channel flow (e.g. Tennekes & Lumley 1967) is given by

$$\frac{dU^+}{dy^+} - \overline{u'v'}^+ = 1 - \frac{y^+}{Re_\tau}, \tag{4.1}$$

and the same expression would be easily found for turbulent pipe flow, as the viscous inner length scale is much smaller than that associated with the boundary curvature at high Reynolds numbers. In the limit of $Re_\tau \to \infty$, (4.1) in the near-wall region (say $y^+ \leqslant 100$) becomes the same as (2.2) because the viscous inner scales are identical to the related Kolmogorov scales in the near-wall region. It is important to remember that both dU^+/dy^+ and $-\overline{u'v'}^+$ in the near-wall region of wall-bounded turbulent shear flow scale very well in the viscous inner units, unlike other statistics such as streamwise and spanwise turbulence intensities, and that they remain constant even if the Reynolds number is sufficiently high (see e.g. the DNS data by Lee & Moser 2015). Therefore, the maximum value of turbulence production in near-wall turbulence is also expected to be around $y^+ \simeq 10$, consistent with the early observations (Tennekes & Lumley 1967), and it should scale very well in the inner units.

4.2. *How large is the turbulence production at Kolmogorov microscale?*

An important outcome of the present study is that turbulence production exists at the Kolmogorov microscale. This mechanism is essentially driven by the local mean shear. However, the reason that this mechanism is unveiled here is essentially because larger eddies are artificially removed. From this viewpoint, it is not very clear whether this turbulence production mechanism would also be active in the presence of larger eddies: indeed, the spectra in full DNSs by Pirozzoli *et al.* (2014) do not show any strong turbulent kinetic energy in the region where the production by Kolmogorov microscale is expected (see figure 8 in Pirozzoli *et al.* 2014). This implies that the production mechanism discovered in the present study may not be very active in the presence of the eddies at all the possible scales.

It is also useful to compute how much energy is dissipated in the present minimal-span simulation, in comparison to that in full simulations. This can be easily obtained by computing skin-friction drag (e.g. Kawahara & Kida 2001). Figure 12 shows variation of skin-friction coefficient of full simulations (Pirozzoli *et al.* 2014) and the present minimal-span simulations on increasing the Reynolds number. As in Hwang (2013) and de Giovanetti *et al.* (2016) for pressure-driven turbulent channel flows, the removal of the motions, the spanwise size of which is greater than $\lambda_z^* > 100 - 140$, leads to a significant amount of skin-friction reduction. Also, the difference of the skin friction generated by the minimal-span simulations from that by full simulations increases, as the Reynolds number increases. This observation also suggests that the production by Kolmogorov microscale in the present numerical experiment is much smaller than that by full simulation. In this respect, it is finally worth mentioning that the Reynolds shear-stress cospectra in a full-scale turbulent flow at high Reynolds numbers were shown to decay with $-7/3$ power law, before it reaches the dissipation range of the spectra (Lumley 1967; Saddoughi & Veeravallit 1994). This indicates that the turbulence production by the eddies at the Kolmogorov microscale would also be insignificant and very small in a full-scale turbulent flow.

4.3. *Above the near-wall region in the minimal unit simulation*

Finally, the present study provides a better understanding for the previous minimal-span simulations for pressure-driven channel flow (e.g. Jiménez & Moin 1991; Jiménez

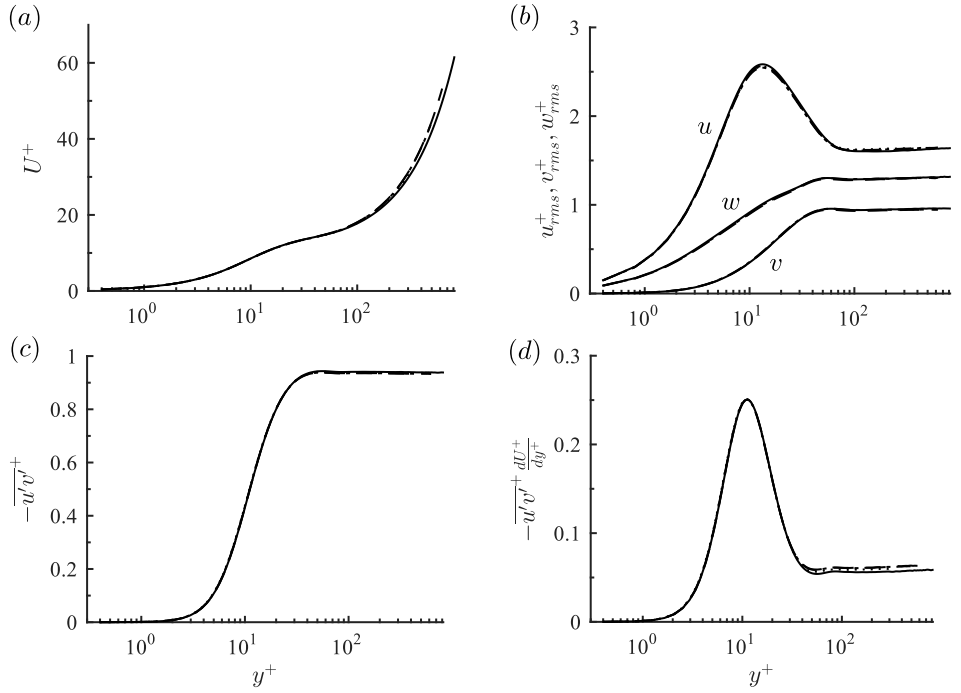

FIGURE 13. Near-wall turbulence statistics: (*a*) $U^+(y^+)$, (*b*) $u^+_{rms}(y^+)$, $v^+_{rms}(y^+)$, $w^+_{rms}(y^+)$, (*c*) $-\overline{u'v'}^+(y^+)$ (*d*) $-\overline{u'v'}^+(y^+)dU^+/dy^+$.

& Pinelli 1999; Hwang 2013). All of these studies have repeatedly reported the presence of a non-negligible amount of turbulent fluctuations above the near-wall region in the minimal-span simulations, even though the spanwise computational domain is not large enough to resolve the large energy-carrying eddies in the logarithmic and outer regions. An explanation for the emergence of such turbulent fluctuations above the near-wall region in the minimal-span simulations was initially proposed by Jiménez & Pinelli (1999), and it starts from turbulence production in the logarithmic region: $\mathcal{P} \sim u_\tau^3/y$. Since the production is roughly balanced with dissipation in the logarithmic region, the decaying vorticity fluctuation in the wall-normal direction would be given, such that: $\omega \sim y^{-1/2}$ from $\mathcal{P} \sim \nu\omega^2$. However, in the minimal-span simulation, the integral length scale above the near-wall region is artificially restricted to be L_z. Therefore, the balance between production and dissipation yields $\omega \sim L_z^{-1/2}$, providing a sound reason for the non-negligible turbulent fluctuation above the near-wall region in the minimal-span simulation.

The present study highlights that this explanation should be based upon the assumption that the production in the minimal-span simulation does not originate from the near-wall region but from the local mean shear. In the case of Couette flow, the uniform mean shear in the bulk region makes the spanwise domain size L_z the precise integral length scale in the bulk region, thereby resulting in turbulence statistics constant in the wall-normal direction. On the other hand, in the case of pressure-driven channel flow, the size of the spanwise domain does not fully represent the integral length scale in the bulk region, as the mean shear is essentially the outcome of the applied pressure gradient – the mean shear in this case decays on approaching from the near-wall to the core region. Therefore, the production mechanism and the resulting turbulent fluctuations

are expected to be gradually weakened, as the wall-normal location moves from the near-wall to the outer region, and this is consistent with the turbulence statistics reported by Hwang (2013). However, it is also important to mention that there should exist the eddies, similar to those observed in the bulk region of the present study, at least just above the near-wall region at sufficiently high Reynolds number, because the mean-momentum balance (4.1) of the pressure-driven channel flow would be identical to (2.2) in the limit of $Re_\tau \to \infty$ in this region. Indeed, the eddy structures and their length scales above the near-wall region in a minimal-span pressure-driven channel flow (Hwang 2013) are remarkably similar to those in the bulk region of the present study. Lastly, it should be stressed that this may indicate the existence of invariant solutions associated with these fluctuations in a pressure-driven channel flow, as in the present Couette flow. However, to the best of our knowledge, the discovery of such invariant solutions is yet to be reported.

Acknowledgements

Q.Y. would like to thank China Scholarship Council for the financial support. Y.H. was supported by the Engineering and Physical Sciences Research Council (EPSRC) in the UK (EP/N019342/1). We also gratefully acknowledge helpful discussions with Prof. J. Christos Vassilicos and Dr. Kengo Deguchi.

Appendix A. Near-wall turbulence statistics of the spanwise minimal Couette flow

The near-wall turbulence statistics of all the LC simulations are reported here. Figure 13 reports first- and second-order turbulence statistics scaled by δ_ν, with which the wall-normal coordinate is given by $y^+ = (y + h)/\delta_\nu$. Consistently with Hwang (2013), all the turbulent statistics show very good agreement at all the Reynolds numbers considered, and they are almost indistinguishable in the near-wall region. One-dimensional spectra of all the velocity components and the Reynolds shear stress are also inspected, as shown in figure 14. Comparison of the spectra from the lowest and the highest Reynolds number clearly suggests that the near-wall turbulence statistics completely scale in the viscous inner units. The spectra also very well charcaterise the typical behaviour of near-wall turbulence (see also Hwang 2013, for further details) – in particular, the streamwise wavenumber spectra of the streamwise velocity shows a peak at $\lambda_x^+ \simeq 600$ and $y^+ \simeq 15$ (figure 14*b*), indicating the near-wall streaks, while those of the wall-normal and spanwise velocities exhibits a peak at $\lambda_x^+ \simeq 200 \sim 300$ and $y^+ \simeq 500$, representing the quasi-streamwise vortices (Jeong *et al.* 1997).

REFERENCES

Bewley, T. R. 2014 *Numerical Renaissance: simulation, optimization, & control*. San Diego: Renaissance Press.

Blackburn, H. M., Hall, P. & Sherwin, S. 2013 Lower branch equilibria in Couette flow: the emergence of canonical states for arbitrary shear flow. *J. Fluid Mech.* **726**, R2.

Chung, D., Chan, L., MacDonald, M., Hutchins, N. & Ooi, A. 2015 A fast direct numerical simulation method for characterising hydraulic roughness. *J. Fluid Mech.* **773**, 418–431.

Deguchi, K. 2015 Self-sustaining states at Kolmogorov microscale. *J. Fluid Mech.* **781**, R6.

Eckhardt, B. & Zammert, S. 2016 Exact coherent structures for the turbulent cascade. *Bulletin of the American Physical Society* **61** (20), A18.008.

Faisst, H. & Eckhardt, B. 2003 Travelling waves in pipe flow. *Phys. Rev. Lett.* **91**, 224502.

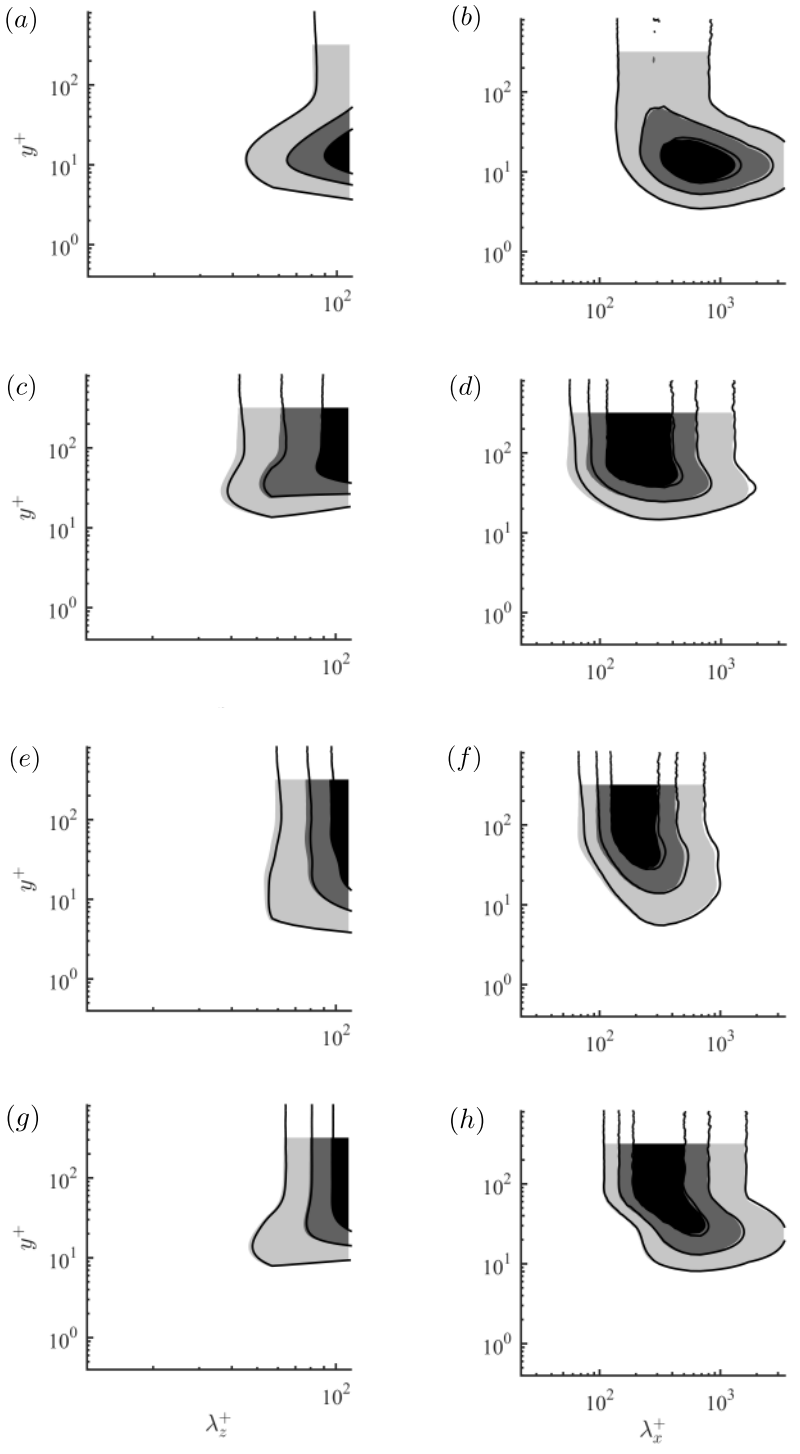

FIGURE 14. Premultiplied one-dimensional (a, c, e, g) spanwise and (b, d, f, h) streamwise wavenumber spectra of (a, b) streamwise velocity, (c, d) wall-normal velocity, (e, f) spanwise velocity and (g, h) Reynolds shear stress. Here: shaded, LC1; solid, LC4. The contour levels are 0.25,0.5 and 0.75 times of each of the maximum.

Flores, O. & Jiménez, J 2010 Hierarchy of minimal flow units in the logarithmic layer. *Phys. Fluids* **22**, 071704.

Gibson, J. F., Halcrow, J. & Cvitanovic, P. 2008 Visualizing the geometry of state space in plane Couette flow. *J. Fluid Mech.* **611**, 107–130.

de Giovanetti, M., Hwang, Y. & Choi, H. 2016 Skin-friction generation by attached eddies in turbulent channel flow. *J. Fluid Mech.* **808**, 511–538.

Hall, P. & Sherwin, S. J. 2010 Streamwise vortices in shear flows: harbingers of transition and the skeleton of coherent structures. *J. Fluid Mech.* **661**, 178–205.

Hall, P. & Smith, F. T. 1991 On strongly nonlinear vortex-wave interactions in boundary-layer transition. *J. Fluid Mech.* **227**, 641–666.

Hamilton, J. M., Kim, J. & Waleffe, F. 1995 Regeneration mechanisms of near-wall turbulence structures. *J. Fluid Mech* **287**, 317–348.

Hwang, Y. 2013 Near-wall turbulent fluctuations in the absence of wide outer motions. *J. Fluid Mech.* **723**, 264–288.

Hwang, Y. 2015 Statistical structure of self-sustaining attached eddies in turbulent channel flow. *J. Fluid Mech.* **723**, 264–288.

Hwang, Y. 2016 Mesolayer of attached eddies in turbulent channel flow. *Phys. Rev. Fluids* **1** (6), 064401.

Hwang, Y. & Bengana, Y. 2016 Self-sustaining process of minimal attached eddies in turbulent channel flow. *J. Fluid Mech.* **795**, 708–738.

Hwang, Y. & Cossu, C. 2010 Self-sustained process at large scales in turbulent channel flow. *Phys. Rev. Lett.* **105**, 044505.

Hwang, Y., Willis, A. P. & Cossu, C. 2016 Invariant solutions of minimal large-scale structures in turbulent channel flow. *J. Fluid Mech.* **802**, R1.

Jeong, J., Benney, F., Schoppa, W. & Kim, J. 1997 Coherent structures near the wall in a turbulent channel flow. *J. Fluid Mech.* **332**, 185–214.

Jiménez, J., Kawahara, G., Simens, M. P., Nagata, M. & Shiba, M. 2005 Characterization of near-wall turbulence in terms of equilibrium and "bursting" solutions. *Phys. Fluids* **17**, 015105.

Jiménez, J. & Moin, P. 1991 The minimal flow unit in near-wall turbulence. *J. Fluid Mech.* **225**, 213–240.

Jiménez, J. & Pinelli, A. 1999 The autonomous cycle of near-wall turbulence. *J. Fluid Mech.* **389**, 335–359.

Jiménez, J. & Simens, M. P. 2001 Low-dimensional dynamics of a turbulent wall flow. *J. Fluid Mech.* **435**, 81–91.

Jiménez, J. & Wray, A. A. 1998 On the characteristics of vortex filaments in isotropic turbulence. *J. Fluid Mech.* **373**, 255–285.

Kawahara, G. & Kida, S. 2001 Periodic motion embedded in plane Couette turbulence: regeneration cycle and burst. *J. Fluid Mech.* **449**, 291–300.

Kim, J. & Moin, P 1985 Application of a fractional-step method to incompressible Navier-Stokes equations. *J. Comp. Phys.* **59**, 308–323.

Kolmogorov, A. N. 1941 The local structure of turbulence in incompressible viscous fluid for very large Reynolds numbers. *Dokl. Akad. Nauk SSSR* **30**, 209–303.

Kolmogorov, A. N. 1991 The local structure of turbulence in incompressible viscous fluid for very large Reynolds numbers. *Proc. R. Soc. London Ser. A* **434**, 9–13.

Lee, M. J., Kim, J. & Moin, P. 1990 Structure of turbulence at high shear rate. *J. Fluid Mech.* **216**, 561–583.

Lee, M. K. & Moser, R. D. 2015 Direct numerical simulation of the turbulent boundary layer over a cube-roughened wall. *J. Fluid Mech.* **774**, p395.

Lumley, J. L. 1967 Similarity and the turbulent energy spectrum. *Phys. Fluids* **10**, 855–858.

MacDonald, M., Chung, D., Hutchins, N., Chan, L., Ooi, A. & Garcia-Mayoral, R. 2017 The minimal-span channel for rough-wall turbulent flows. *J. Fluid Mech.* **816**, 5–42.

Marusic, I., McKeon, B. J., Monkewitz, P. A., Nagib, H. M., Smits, A. J. & Sreenivasan, K. R. 2010 Wall-bounded turbulent flows at high Reynolds numbers: Recent advances and key issues. *Phys. Fluids* **22**, 065103.

Mizuno, Y. & Jiménez, J. 2013 Wall turbulence without walls. *J. Fluid Mech.* **723**, 429–455.

Nagata, M. 1990 Three-dimensional finite-amplitude solutions in plane Couette flow: bifurcation from infinity. *J. Fluid Mech.* **217**, 519–527.

Park, J. S. & Graham, M. D. 2016 Exact coherent states and connections to turbulent dynamics in minimal channel flow. *J. Fluid Mech.* **782**, 430–454.

Pirozzoli, S., Bernardini, M. & Orlandi, P. 2014 Turbulence statistics in Couette flow at high Reynolds number. *J. Fluid Mech.* **758**, 327–343.

Rawat, S., Cossu, C., Hwang, Y. & Rincon, F. 2015 On the self-sustained nature of large-scale motions in turbulent Couette flow. *J. Fluid Mech.* **782**, 515–540.

Robertson, J. M. 1959 On turbulent plane Couette flow. In *Proceedings of the Sixth Midwestern Conference on Fluid Mechanics*, pp. 169–182.

Saddoughi, S. G. & Veeravallit, S. V. 1994 Local isotropy in turbulent boundary layers at high reynolds number. *J. Fluid Mech.* **268**, 333–372.

Schoppa, W. & Hussain, F. 2002 Coherent structure generation in near-wall turbulence. *J. Fluid Mech.* **453**, 57–108.

Sekimoto, A., Dong, S. & Jiménez, J. 2016 Direct numerical simulation of statistically stationary and homogeneous shear turbulence and its relation to other shear flows. *Phys. Fluids* **28**, 035101.

Tennekes, H. & Lumley, J. L. 1967 *A first course in turbulence*. MIT Press.

Vassilicos, J. C. 2015 Dissipation in turbulent flows. *Annu. Rev. Fluid Mech.* **47**, 95–114.

Waleffe, F. 1997 On a self-sustaining process in shear flows. *Phys. Fluids* **9**, 883–900.

Waleffe, F. 2001 Exact coherent structures in channel flow. *J. Fluid Mech.* **435**, 93–102.

Wedin, H. & Kerswell, R. R. 2004 Exact coherent structures in pipe flow: travelling wave solutions. *J. Fluid Mech.* **508**, 333–371.

Willis, A. P., Cvitanovic, P. & Avila, M. 2013 Revealing the state space of turbulent pipe flow by symmetry reduction. *J. Fluid Mech.* **721**, 514–540.

Willis, A. P., Cvitanovic, P. & Avila, M. 2016 Symmetry reduction in high dimensions, illustrated in a turbulent pipe. *Phys. Rev. E* **93**, 022204.